Seismic Modelling in 3D for Migration Testing

Gary F. Margrave and Joanna K. Cooper

ABSTRACT

A 3D modelling technique, called Rayleigh-Sommerfeld modelling, is described as an alternative to Kirchhoff modelling. Rayleigh-Sommerfeld modelling, when applied using a forward Born approximation, is shown to be the familiar phase-shift migration running in reverse. Compared to the Kirchhoff method, Rayleigh-Sommerfeld is much faster, especially on large datasets, but produces a similar response. Rayleigh-Sommerfeld is used to create an exhaustive 3D synthetic dataset which will be used for 3D migration testing. Such an exhaustive dataset, defined as having no spatial aliasing in either source or receiver gathers, can be extremely large and the efficiency of Rayleigh-Sommerfeld modelling is required to create one. The model created is the response of three horizontal reflectors embedded in a v(z) medium. Consisting of 1681 source gathers, each having 1681 receivers, it is shown to be very high frequency and to contain both specular reflections and diffractions. Example 3D shot record migrations demonstrate the fidelity of the model and the high resolution of prestack migration.

INTRODUCTION

Seismic modelling plays a major role in seismic exploration and, very frequently, finite-difference algorithms are the tool of choice. This is because the finite-difference method can produce a very realistic response and the underlying earth model can be as highly variable as the real world. However, the method has significant problems, foremost among these being the high computational cost and the presence of significant grid dispersion. These two drawbacks usually compound one another in that the way to reduce grid dispersion is either to reduce the time-step, or to increase the order of the spatial differences, or both; these strategies all increase computational cost. Consequently, 3D finite difference modelling is often so severely limited by the required computational burden that the resulting temporal frequency bandwidth is restricted to much less than comparable real datasets. This is especially true if an entire seismic survey, consisting possibly of hundreds or thousands of source records, is to be simulated. A common fallback position is to use a raytracing code but then one is generally required to accept a model without diffractions, that is with only specular reflections. This can be an unacceptable limitation as often the modelled data is intended to be migrated. Indeed, the primary purpose of creating the data may be to test an imaging algorithm. Kirchhoff modelling is often seen as the extension of raytrace modelling to include diffractions; however, this comes at a much higher cost as each reflecting surface must be integrated across for each source-receiver pair.

Here we report on the creation of an exhaustive 3D synthetic seismic dataset by a technique which we will call Rayleigh-Sommerfeld modelling. By "exhaustive" we mean a dataset sampled sufficiently in both source and receiver positions that neither common source gathers nor common receiver gathers have any significant spatial aliasing. This is important because our primary purpose is to study the 3D acquisition footprint and we postulate that much of that footprint arises from spatially aliased data.

Our paper begins with a detailed discussion of the concept of the exhaustive dataset, with special attention to the relationship between maximum frequency, velocity, and the spatial sample sizes needed to avoid aliasing. Subsequently we develop Rayleigh-Sommerfeld modelling and show that it is simply phase-shift migration in reverse. We discuss the links between Rayleigh-Sommerfeld modelling, Kirchhoff modelling, and the Born approximation. Finally, we conclude with examples of our modelled seismic data and discuss the computational cost compared to other methods. We show that this method is an effective 3D modelling technique capable of producing very high frequency responses but with no multiples, surface waves, interface waves or similar phenomena.

THE EXHAUSTIVE DATASET

Temporal aliasing is nearly nonexistent in seismic data recording and processing because the data are usually passed through an analog (i.e. non-digital) low-pass filter that rejects frequencies above the Nyquist frequency, $f_N = \left(2\Delta t\right)^{-1}$, defined by the chosen temporal sample interval, Δt. Usually such an *antialias filter* will actually begin rejection at 60%-80% of f_N in order to reach maximum rejection for all frequencies greater than f_N. However, spatial sampling, defined by the locations of sources and receivers, is inherently discrete and it is not generally possible to record and process a continuous signal in space prior to sampling. For this reason, most seismic datasets suffer from a considerable degree of spatial aliasing. In the best situations, usually only slow moving coherent noises show significant aliasing but, all too often, signal is also aliased.

Modern seismic datasets are commonly 5D volumes, requiring two spatial dimensions to specify receiver locations, two more for source locations, and the fifth dimension is, of course, time (apologies to Einstein!). The assessment of spatial aliasing requires the specification of a spatial ensemble, with its consequent spatial sampling, and many such ensembles can be found in the 5D volume. The most obvious ensembles, or gathers, are *common source* (i.e. all traces recorded with a single source), *common receiver* (all traces recorded at a fixed receiver from any source), *common offset* (all traces with a fixed source-receiver offset, either vector or scalar), and *common midpoint* (all traces having the same source-receiver midpoint). Many more ensembles can be defined and all typically have characteristic spatial sample sizes. A particular seismic event may be spatially aliased in one ensemble but not in another. Here we shall primarily be concerned with the common source and common receiver gathers, for which the spatial sample intervals are the receiver spacing and the source spacing respectively. The common source gather is the only ensemble that represents a single physical wavefield and is the ensemble of actual recording. Common receiver gathers are typically formed during data processing for reasons relating to the compositing of multiple source gathers into the final seismic image.

Definition: An exhaustive seismic dataset is one which shows no significant spatial aliasing in either common source or common receiver gathers.

Of course, an exhaustive dataset may be aliased in other gathers but we will not pursue this point. That an exhaustive dataset is even possible, given the impossibility of

continuous spatial recording, is the consequence of the temporally bandlimited nature of the data and the physical phenomenon of evanescence. Many seismic datasets are temporally bandlimited because they were recorded with a bandlimited source such as vibroseis. However, even if dynamite was used, which can generate very high frequencies, temporal band limiting still occurs because of the antialias filters used in temporal sampling and described above. The vibroseis bandlimit imposed by the highest frequency is a limitation upon the *signal band* while the antialiasing bandlimit is a limitation upon both signal and background noise. Put another way, prudent acquisition parameter selection usually has the temporal Nyquist at least twice as large as the highest sweep frequency, even though any frequencies higher than the swept band will contain minimal signal. It is the highest signal frequency that is of concern here, not the Nyquist frequency, and we denote that highest signal frequency $f_{\max}$.

Surface seismic acquisition will be assumed here to occur on the plane z=0. Such recorded data can be directly analyzed for its temporal frequency spectrum and the spectra of the two horizontal wavenumbers. Denoting these as f, k_x, and k_y respectively, the vertical wavenumber, k_z, can be calculated from the scalar wave dispersion relation

$$k_z = \sqrt{\frac{f^2}{v^2} - k_x^2 - k_y^2} \tag{1}$$

where v is the wavespeed. The surface recording can then be downward continued by application in the (f, k_x, k_y) domain of the multiplication operator

$$\hat{W} = \begin{cases} \exp(ik_z\Delta z), & \dfrac{f^2}{v^2} \geq k_x^2 + k_y^2 \\[2mm] \exp(-|k_z|\Delta z), & \dfrac{f^2}{v^2} < k_x^2 + k_y^2 \end{cases}, \tag{2}$$

where Δz denotes the size of the downward step. The dual nature of the extrapolation operator in equation (2) is a mathematical statement of the phenomenon of evanescent waves. Essentially, propagating waves are restricted to the cone described by $\dfrac{f^2}{v^2} \geq k_x^2 + k_y^2$ while the exterior of this cone refers to Fourier components that are exponentially damped in the z direction. Thus, it follows that, for temporally bandlimited data, all wavenumbers such that $k_x^2 + k_y^2 > \dfrac{f^2}{v^2}$ will be exponentially damped and of no consequence in subsurface imaging. Thus, if the spatial sample rates are such that $(2\Delta x)^{-1} > f_{\max}v^{-1}$ and $(2\Delta y)^{-1} > f_{\max}v^{-1}$, then there will be no significant spatial aliasing. Taking $\Delta x = \Delta y$, a square sampling lattice requires

$$\Delta x \le \frac{v}{2f_{\max}} \tag{3}$$

in order that spatial aliasing be negligible.

The analysis in the previous paragraph needs further consideration for a real setting with variable velocity and surface waves. Generally the near-surface layer has a much lower seismic wavespeed than any deeper layer. Indeed, very slow P-wave speeds, often of the order of 1000 m/s or less, are commonly found and S-wave speeds are even slower. Given a typical $f_{\max}$ of 100Hz, then 1000 m/s demands a spatial sample interval of 5 m, which is clearly very demanding. Since our concern here is numerical modelling, and our technique does not automatically generate such slow waves, it will prove sufficient to use a subsurface velocity to determine the spatial sample interval. In real data acquisition, it is often the case that surface waves and other coherent noises are aliased while deeper reflection events (signal) are not.

An exhaustive dataset must have spatial sample intervals that conform to inequality (3) in all four of its spatial dimensions. Assume that a model is to be constructed where the source and receiver lattices are identical and consist of a square grid with spacing Δx and having area L^2, where L is the size of the square, or aperture. Then the exhaustive survey will require $(L/\Delta x)^2$ receivers and the same number of sources. Thus the number of seismic traces in such a model is

$$n_{tr} = \left(\frac{L}{\Delta x}\right)^4 \tag{4}$$

or, adopting the equality in relation (3) gives

$$n_{tr} = \left(\frac{2f_{\max}L}{v}\right)^4. \tag{5}$$

The fourth power here means that the number of traces required for an exhaustive dataset can rapidly become too large to contemplate. Table 1 shows the number of traces required for an exhaustive dataset (in millions) as a function of a variety of apertures and sample sizes.

Table 1. The number of traces required for an exhaustive survey of size L^2 having square spatial sample size of Δx. Trace numbers are given in millions.

$\Delta x \downarrow \quad L \rightarrow$	2000	1000	500	250	125
40	6.25	0.39	0.024	0.0015	10^{-4}
20	100	6.25	0.39	0.024	0.0015
10	1600	100	6.25	0.39	0.024
5	2560	1600	100	6.25	0.39
2.5	409600	2560	1600	100	6.25

In a real setting, an exhaustive dataset of any significant aperture is nearly always impossible. This is because seismic velocities are generally very slow for shallow layers and equation (5) has velocity in the denominator. If waves in the slowest shallowest layers are to be sampled without aliasing, then as shown in Figure 1, the number of traces required, for even a modest survey, is in the billions. Since usually the slowest waves are some form of coherent "noise", a real dataset usually has aliased noise even if the reflection signal from target zones is not aliased. This same limitation applies to synthetic datasets produced with finite-differencing or similar techniques since these methods generally generate all possible waves. In the modelling technique to be described here, only primary reflections from designated reflectors are generated and so an exhaustive dataset is much more possible.
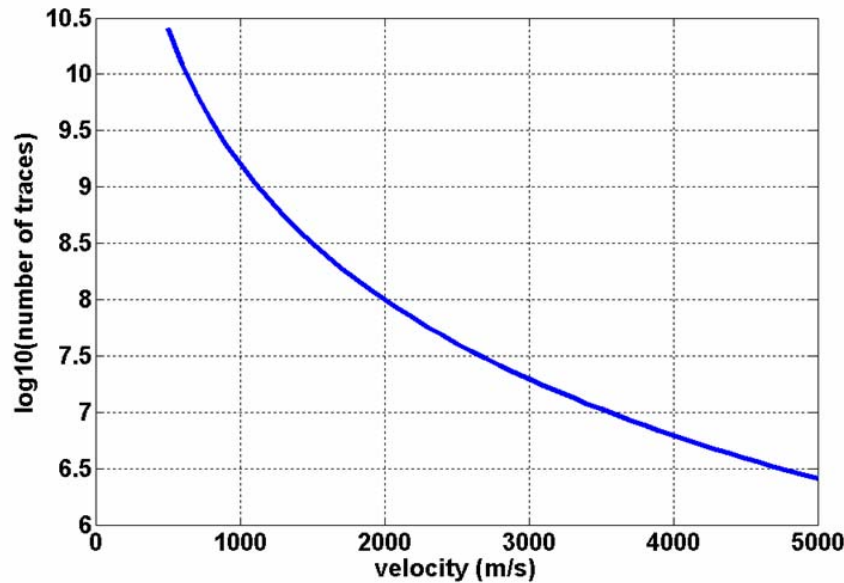
FIG. 1. The logarithm of the number of traces required to form an exhaustive 3D dataset is shown versus velocity. Assumed here are a maximum frequency of 100 Hz and an aperture of 1 km.

RAYLEIGH-SOMMERFELD MODELLING

For the purpose of testing migration algorithms, a modelling method should be capable of a very high-frequency response and must produce diffractions. It is not essential that the method generate multiples or that it correctly model the variation of reflection strength with incidence angle. Furthermore, to generate an exhaustive dataset, a numerically efficient method is required. These considerations argue directly against finite-difference modelling since a high-frequency finite-difference result takes a great computational effort. Furthermore, the completeness of the finite-difference wavefield is not required. Conventional asymptotic ray theory, while computationally very efficient, was also judged not acceptable because of the difficulty in producing diffraction effects. This led to a consideration of Kirchhoff modelling (e.g. Schearer, 1999) because it is able to naturally generate both diffractions and specular reflections as emergent properties (i.e. stationary phase contributions). However, as will be seen shortly, Kirchhoff modelling is

computationally $O\left(N^2\right)$, where $N = n_x n_y$ is the number of grid points on the reflector (or on the surface), and this leads to enormous compute times for even small models. Finally, we converged on Rayleigh-Sommerfeld diffraction theory for which our primary reference is Ersoy (2007, chapter 4). Again, as will be seen, this diffraction theory is very nearly as accurate as that of Kirchhoff and is $O\left(N \log N\right)$. While it is expected that the average geophysicist may be unfamiliar with the phrase "Rayleigh-Sommerfeld diffraction theory" it turns out that the technique is just the familiar phase-shift migration run backwards. The following presentations of Kirchhoff diffraction theory and Rayleigh-Sommerfeld diffraction are both taken from Ersoy (2007). The derivations are not given here and the reader is referred to that text for details.
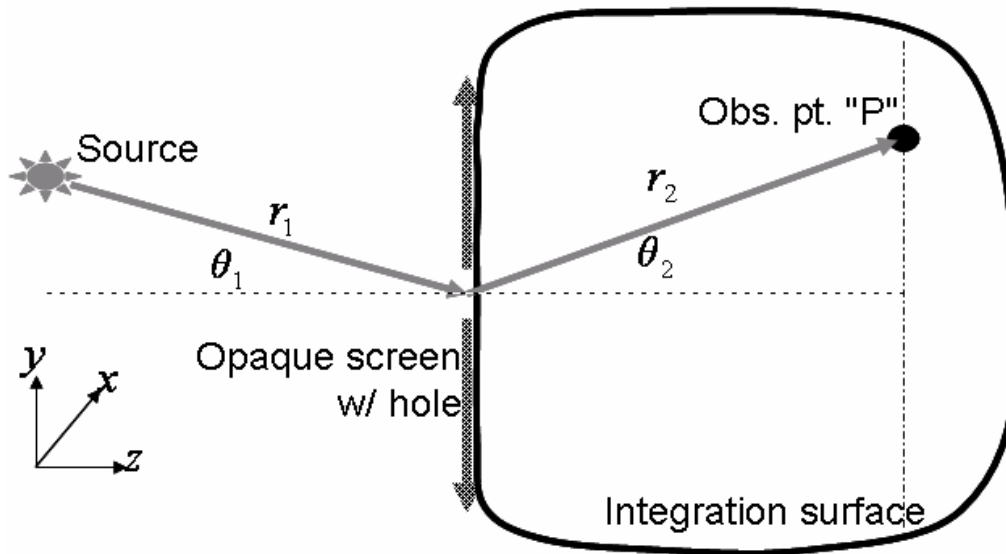
FIG. 2. The geometry relevant to the derivation of the Kirchhoff diffraction formula for the classic case of an opaque screen with a hole.

Figure 2 shows the basic geometry for the derivation of the Kirchhoff diffraction formula for the case of scalar waves that impact from the left on a perfectly opaque screen with a perfectly transparent hole and then subsequently are observed at a point P, which is taken to be on a plane to the right of the screen. The screen is assumed to be of infinite extent and the medium excluding the screen is taken to be homogeneous. Two basic results from mathematical physics, Green's theorem and the Sommerfeld radiation condition, are then invoked. The former is simply a generalization of the fundamental theorem of calculus from 1D to 3D, while the latter describes the physical constraint that we may have only outgoing energy at infinity. Green's theorem relates the integral of a second-order differentiated scalar field over a volume to the integral of the normal derivative of that field over the surface bounding the volume. This is directly analogous to the fundamental theorem of calculus in 1D which relates the integral of a function over a line segment to the evaluation of the anti-derivative of that function at the end points of the line segment. In Figure 2, the volume of integration is formed by taking a finite, circular portion of the right-hand-side of the screen, centered over the hole and a corresponding hemisphere to the right and then letting the radius of the circle/hemisphere

recede to infinity. We denote the surface of this infinite volume by Σ. The scalar field of concern, ψ, is assumed to satisfy the homogenous media Helmholtz equation for a point source placed at the source location. The result is that the field at the observation point, $\psi(\underline{x} = \underline{P})$ ($\underline{x}$ is a general position vector while $\underline{P}$ is the specific vector pointing to the observation point), is given by

$$\psi(\underline{x} = \underline{P}) = \frac{1}{4\pi} \int_\Sigma \left[G \frac{\partial \psi}{\partial n} - \psi \frac{\partial G}{\partial n} \right] d\underline{s} \tag{6}$$

where G is the Green's function for a source placed at the observation point, $\underline{s} \in \Sigma$, and the differentiation is taken in the direction of the outward normal to Σ. Then the Sommerfeld radiation condition may be invoked to show that the contribution to the integral in equation (6) from the infinite hemisphere vanishes, leaving only the integral over the screen, S, which is

$$\psi(\underline{x} = \underline{P}) = \frac{1}{4\pi} \int_S \frac{e^{ikr_2}}{r_2} \left[\frac{\partial \psi}{\partial n} - ik \cos(\theta_2) \psi \right] d\underline{s} \tag{7}$$

where $G = \exp(ikr_2)/r_2$ has been used and $k = 2\pi f / v$, with f being frequency and v being wavespeed. Also in equation (7), only the far-field term has been kept when evaluating the normal derivative of G. The further evaluation of equation (7) requires knowledge of the field ψ and its normal derivative at all points on the right hand side of the screen. Here Kirchhoff made the approximation that the field and normal derivative on the opaque portion of the screen are both zero while in the aperture of the hole, denoted A, the field and normal derivative are precisely what would be expected from a point source if there were no screen at all. Under this approximation, and again invoking a far-field approximation in the normal derivative, the usual Kirchhoff expression is

$$\psi(\underline{x} = \underline{P}) = \frac{ik}{4\pi} \int_S \frac{e^{ik(r_1+r_2)}}{r_1 r_2} \left[\cos(\theta_1) - \cos(\theta_2) \right] \rho(\underline{s}) d\underline{s} \tag{8}$$

where we have defined

$$\rho(\underline{s}) = \begin{cases} 1, & \underline{s} \in A \\ 0, & \underline{s} \notin A \end{cases}. \tag{9}$$

The reason for defining the function $\rho(\underline{s})$ rather than simply restricting the domain of integration to the aperture, A, is to facilitate the generalization of equation (8) to the reflection seismic case. To this end, we simply fold Figure 2 at the screen, which becomes the reflector, to identify the source plane with the recording plane, and we allow $\rho(\underline{s})$ to generalize to the reflection coefficient of the "reflector". Thus our reflection seismic Kirchhoff formula is

$$\psi\left(\underline{x}_r, \underline{x}_s\right) = \frac{ik}{4\pi} \int_s \frac{e^{ik(r_1+r_2)}}{r_1 r_2} \left[\cos\left(\theta_1\right) + \cos\left(\theta_2\right)\right] \rho\left(\underline{s}\right) d\underline{s} \tag{10}$$

where r_1 is the distance from the source (at $\underline{x}_s$) to a point on the reflector, r_2 is the distance from the receiver (at $\underline{x}_r$) to a point on the reflector, θ_1 is the angle of raypath from the source at the reflector, θ_2 is the angle from the reflector to the receiver and is π greater than θ_2 in equation (8), and, $\rho\left(\underline{s}\right)$ is no longer given by equation (9), but is instead allowed to take any value in the interval $\left[-1,1\right]$. Before discussing the Rayleigh-Sommerfeld theory, we mention that the integration in equation (10) must be conducted over the entire reflection surface for each source-receiver pair. Considering the case of a fixed source position into an exhaustive set of receivers, we let the number of points in the 2D source-receiver plane be *N*, and assume that the reflector is also gridded with *N* points. Thus the cost of the integral itself is $O\left(N\right)$ but it must be computed *N* times so that the cost of a source gather is $O\left(N^2\right)$.

The derivation of the Rayleigh-Sommerfeld diffraction integral follows a similar pattern with the major difference being that the Green's function used is not just that for a point source at the observation location, rather, *G* is taken as the difference between the Green's functions for a source at the observation point and for a mirror image source at the corresponding point on the other side of the screen. The result is that the $\partial\psi/\partial n$ term in equation (6) is cancelled and, after some calculation, we obtain

$$\psi\left(\underline{x} = \underline{P}\right) = \frac{1}{4\pi} \int_s \psi \frac{\partial}{\partial z}\left(\frac{e^{ikr_2}}{r_2}\right) d\underline{s} \tag{11}$$

where the z direction is orthogonal to the screen. The integration in equation (11) is actually a convolution over the screen, a fact which can be appreciated by noting that

$$r_2 = \sqrt{\left(x_s - x_p\right)^2 + \left(y_s - y_p\right)^2 + \left(z_s - z_p\right)^2} \tag{12}$$

where the observation point coordinates are $\left(x_p, y_p, z_p\right)$ and the screen coordinates are $\left(x_s, y_s, z_s\right)$. Then, with $\psi = \psi\left(x_s, y_s, z_s\right)$ and $d\underline{s} = dx_s dy_s$, equation (11) becomes recognizable as a convolution of the wavefield on the screen with the function

$$W\left(x, y, z\right) = \frac{\partial}{\partial z}\left(\frac{e^{ikr_2}}{r_2}\right) = \int_s e^{iz\sqrt{k^2 - k_x^2 - k_z^2}} e^{i\left(k_x x + k_y y\right)} dk_x dk_y . \tag{13}$$

That is, the wavefield is convolved with the function *W* which is the *z* derivative of the Green's function. The last form given for *W* is not at all obvious but is well-known from imaging theory and identifies *W* as the extrapolator for scalar waves. If the Kirchhoff approximation (see discussion preceding equation (8)) is now made for the field on the screen, then we can write equation (11) as

$$\psi\left(\underline{x} = \underline{P}\right) = \frac{1}{4\pi} \int_S \psi_o\left(x_s, y_s, z_s\right) W\left(x_p - x_s, y_p - y_s, z_p - z_s\right) \rho\left(\underline{s} = \left(x_s, y_s\right)\right) d\underline{s} \quad (14)$$

where ψ_0 is the field from a point source evaluated on the screen and $\rho\left(\underline{s}\right)$ is given by equation (9). As was done previously, we generalize to the seismic reflection case by simply interpreting $\rho\left(\underline{s}\right)$ as the reflectivity function on the reflector and identifying the source and image planes with each other. Since equation (14) is a convolution, we can express it in the Fourier domain as

$$\psi\left(\underline{x}_r, \underline{x}_s\right) = \frac{1}{4\pi} \int_S \widehat{W}\left(k_x, k_y, z_p - z_s\right) \widehat{\psi_o \rho}\left(k_x, k_y, z_s\right) e^{ik_x x + ik_y y} dk_x dk_y \quad (15)$$

where the "hats" indicate 2D Fourier transforms over *x* and *y*. Now it is apparent that the Rayleigh-Sommerfeld diffraction theory is just modelling by running the familiar phase-shift migration backwards. Equation (15) states that the field of the source is evaluated at the reflector, ψ_0, and then multiplied by the reflectivity function, ρ. This product is then Fourier transformed, multiplied by the phase-shift operator $\widehat{W}$, and inverse Fourier transformed. Furthermore, since ψ_0 can be computed as the source response extrapolated to the reflector, we have the algorithm

$$\psi\left(\underline{x}_r, \underline{x}_s\right) = \mathbf{F}^{-1}\widehat{W}\mathbf{F}\rho\mathbf{F}^{-1}\widehat{W}\mathbf{F}\psi_{source} \quad (16)$$

where $\mathbf{F}$ is the 2D Fourier transform. Thus the algorithm is: (1) phase shift the source wavefield to the reflector, (2) multiply by the reflectivity function, (3) phase shift the result of (2) back to the surface. This is illustrated in Figure 3 and Figure 4. In contrast to equation (8), which must be evaluated independently at a cost of $O\left(N\right)$ for each of N receivers for a cost of $O\left(N^2\right)$, equation (16) gives a result for all receivers simultaneously. Since this is accomplished entirely with Fourier transforms, the computational effort is $O\left(N \log N\right)$.

There is an alternate formulation for Rayleigh-Sommerfeld modelling, also described by Ersoy (2007), called Rayleigh-Sommerfeld II, that is worth mentioning. To derive this expression, a Green's function which is the sum, rather than the difference, of a source at the receiver location and its mirror image is used. The result is an expression similar to equation (11) but in which the *z* derivative is applied to the field not to the Green's function. Ersoy comments that the average of the two Rayleigh-Sommerfeld expressions has been shown to be equal to the Kirchhoff formula.
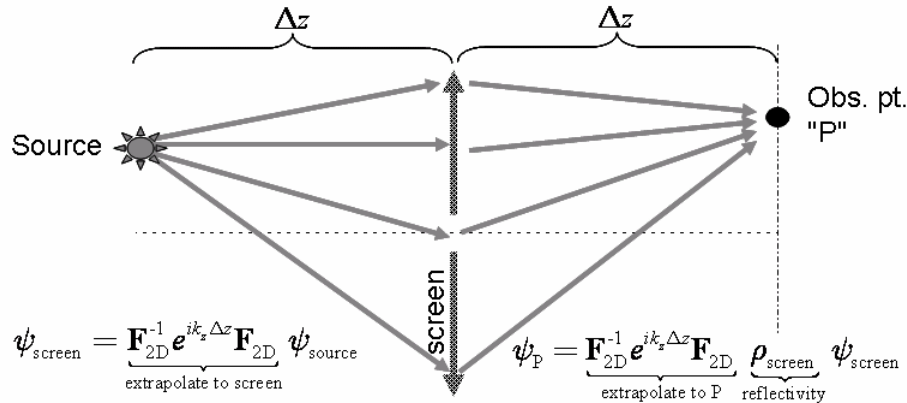
FIG. 3. Rayleigh-Sommerfeld modelling is depicted as described by equation (16). The source wavefield is extrapolated by phase shift to the screen. At the screen it is multiplied by the function ρ describing the "transmissivity" of the screen, and then it is phase-shifted to the observation plane.
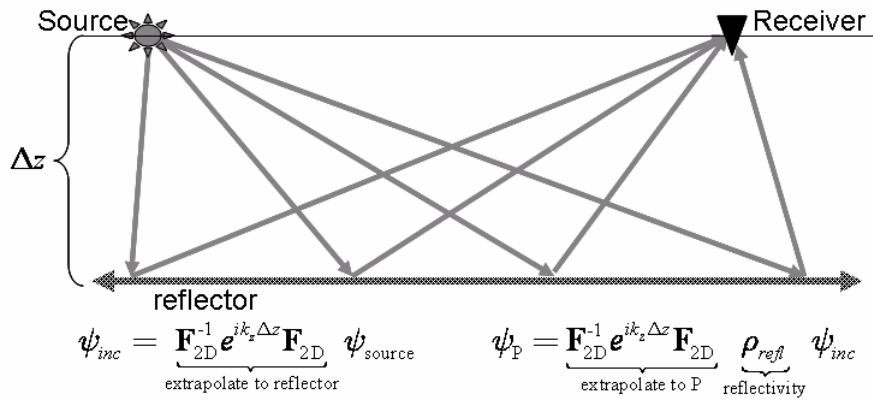

FIG. 4: Rayleigh-Sommerfeld modelling applied to the seismic reflection case. Here the screen of Figure 3 becomes the reflector and the screen transmissivity becomes the reflectivity. Also the source and observation planes become identical.

Although the Kirchhoff and Rayleigh-Sommerfeld theories are called "diffraction theories" they actually compute the entire response of the reflector and so include the specular component as well. While the Rayleigh-Sommerfeld formula is much faster than the Kirchhoff one, the latter easily adapts to circumstances such as a non-horizontal reflector while the former does not. Also, as developed here, both theories do not include the variation of reflection coefficient with incidence angle. This is somewhat easier to accommodate with Kirchhoff theory since raytracing must be done anyway to obtain the incidence angles. In the Rayleigh-Sommerfeld case, it would still be possible to include this effect by separately raytracing the incidence angles.

Both theories can be extended in the same approximate way to a multi-reflector setting. For this case, the first-order Born approximation can be adopted, which means (i) the reflectivity and the background velocity model are considered to be decoupled (independent), (ii) the background velocity model is taken to be smooth and describes wave propagation (iii) the reflectivity is only non-zero on reflecting surfaces, and (iv)

only primary reflections are generated. With these considerations, the response of a multi-reflector model is

$$\psi\left(\underline{x}_r,\underline{x}_s\right)= \sum_{k=1}^{N_{reflectors}} \mathbf{F}^{-1}\widehat{W_k}\mathbf{F}\rho_k\mathbf{F}^{-1}\widehat{W_k}\mathbf{F}\psi_{source} \qquad (17)$$

where ρ_k is the reflectivity, and $\widehat{W}_k$ is the WKBJ phase shift extrapolator appropriate for the kth reflector given the background velocity mode. While transmission coefficients are not explicitly included here they can be made a part of $\widehat{W}_k$.

APPLICATION

It was desired to create an exhaustive dataset for the purpose of studying the 3D acquisition/imaging footprint. After consideration of the available computing resources and the technical requirements of the study, a survey of 400m by 400m sampled at 10 m was chosen. This means that there are $41^2 = 1681$ receivers and the same number of sources, and $41^4 = 2825761$ traces. Figure 5 shows the velocity model, which was chosen to be laterally invariant (to conform with the phase-shift formulation of Rayleigh-Sommerfeld modelling), and which was constructed to have a low velocity surface layer as is typical for land surveys. The data was modelled with an impulsive source and subsequently bandlimited with Ormsby[1] parameters of [0 0 110 180] Hz. This means that the primary signal band was 0->110 Hz. Three horizontal reflectors were modelled at depths of 100, 180, and 200 m. The first two reflectors were featureless with constant reflection coefficients of -.05 and +.05 respectively. The third reflector contained a channel model, shown in Figure 6, with reflection coefficients of +0.1 outside the channel and -0.1 inside the channel. There were also 6 point scatterers embedded in the third reflector. This information is summarized in Table 2.

Table 2. Velocity, depth, and reflector information for the model are shown.

Depth (meters)	Velocity (m/sec)	Reflector	Comment
0	1200		
20	2200		
100	2400	first	r.c.=-0.05
180	2800	second	r.c.=+0.05
190	3000		
200	3000	third	Figure 6
500	3000		

---

[1] Although we specify our filter with Ormsby parameters, the actual implementation in our software has a Gaussian taper with rounded corners.
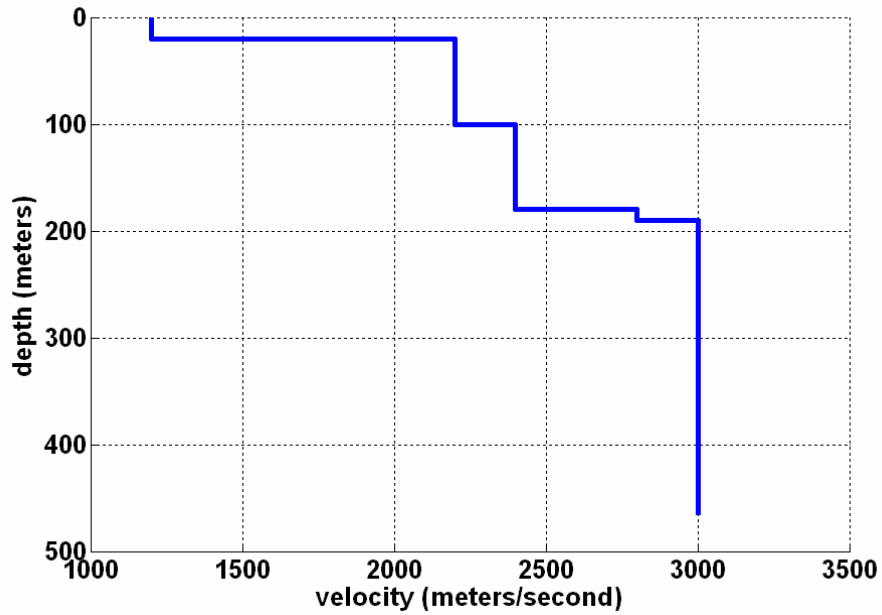
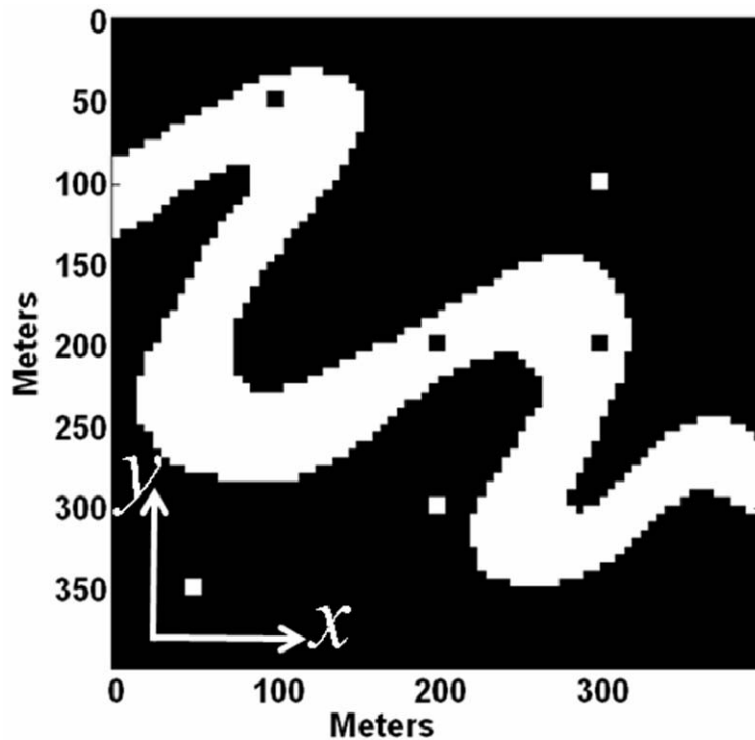FIG. 5. The velocity model chosen for the exhaustive dataset.

FIG. 6. The third reflector, placed at a depth of 200 m in the model. The black color corresponds to a reflection coefficient of +0.1 while white is -0.1.

The spatial sampling was chosen such that a ray with an reflection angle of 90º on the first reflector will just lie on the boundary of spatial aliasing at 110 Hz. To appreciate this, it is instructive to calculate the critical frequency, that is the frequency at which

spatial aliasing begins, for a 90º ray from each reflector assuming the 10 m sample interval. Since such a ray propagates to the surface while conserving its horizontal slowness (Snell's law), a simple calculation shows that this critical frequency is given by $f_{crit} = v_+ / (2\Delta x)$, where v_+ is the velocity immediately above the reflector. For the first second and third reflectors, v_+ is 2200 m/s, 2400 m/s, and 3000 m/s and the resulting critical frequencies are 110 Hz, 120 Hz, and 150 Hz. respectively. Thus only frequencies in the Ormsby taper will suffer any aliasing and, for the third reflector this is quite minimal, and will correspond only to very large scattering angles.

Since this model is to be used for migration testing, the receiver data recorded on the 10m grid will be downward extrapolated to each reflector and examined. From a traditional perspective of NMO correction and CMP stack, the receivers on a 10m grid sample the reflector in the subsurface on a 5m grid. To accommodate this effect the reflectors were all specified on a 5m grid and the complete 3D Rayleigh-Sommerfeld response was computed on that finer grid. Thus the wavefields were actually computed on an 81x81 grid and every other trace was saved to simulate the receivers recording on a 41x41 grid.

As a first example of calculated responses, Figure 7 compares Rayleigh-Sommerfeld modelling and Kirchhoff modelling. Each panel is a time slice through the 3D response of a single shot. The complicated reflection response is due to the channel. The times beside each panel are representative CPU times. The $O(N^2)$ scaling for Kirchhoff is the reason for the huge change in run times when the grid spacing is halved. It seems that Kirchhoff modelling is slightly superior to Rayleigh-Sommerfeld at the same grid spacing; however, the difference in computation times is dramatic. It is obviously preferable to use Rayleigh-Sommerfeld on a fine grid whenever the limitations of the technique are acceptable.
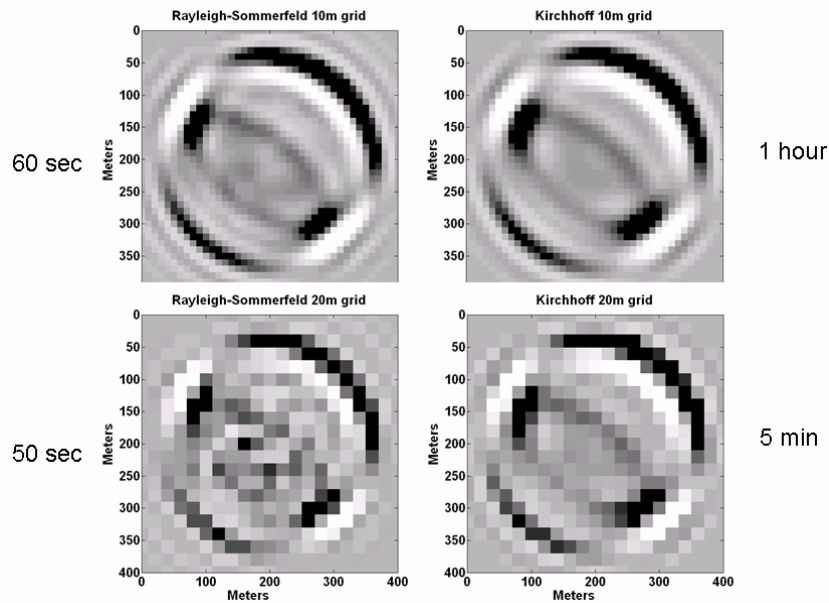
FIG. 7. Rayleigh-Sommerfeld modelling compared to Kirchhoff at two different grid spacings. Each panel is a constant-time slice through a 3D response.

Figure 8 displays an entire 3D source record for a source in the geometric center of the survey (x = y = 200 m on Figure 6). The record is displayed as a 2D array in which each y-line is identifiable by the hyperbolic reflection signatures of the three reflectors. The featureless first reflector manifests as a sequence of white hyperbolae occurring at delays which are minimal in the center of the figure. The featureless second reflector is similarly structured but is at overall greater delays corresponding to its greater depth. The two reflectors also have reflection coefficients of opposite sign. The third reflector is much more complicated and shows an intricate mix of reflection and diffraction effects. Figures 9 and 10 show an x-line and a y-line sorted from the data of Figure 8; the two lines cross at the source location. Comparison with Figure 6 allows for the identification of channel edge diffractions, channel reflections, and off-channel reflections. In general the diffraction events are quite complicated, possibly because there are strong out-of-the-plane effects from the sinuous channel. Figure 11 is a time slice through the 3D source record, demonstrating a nice circular (non-dispersive) wavefront, and Figure 12 shows a 3D perspective view of the source record.
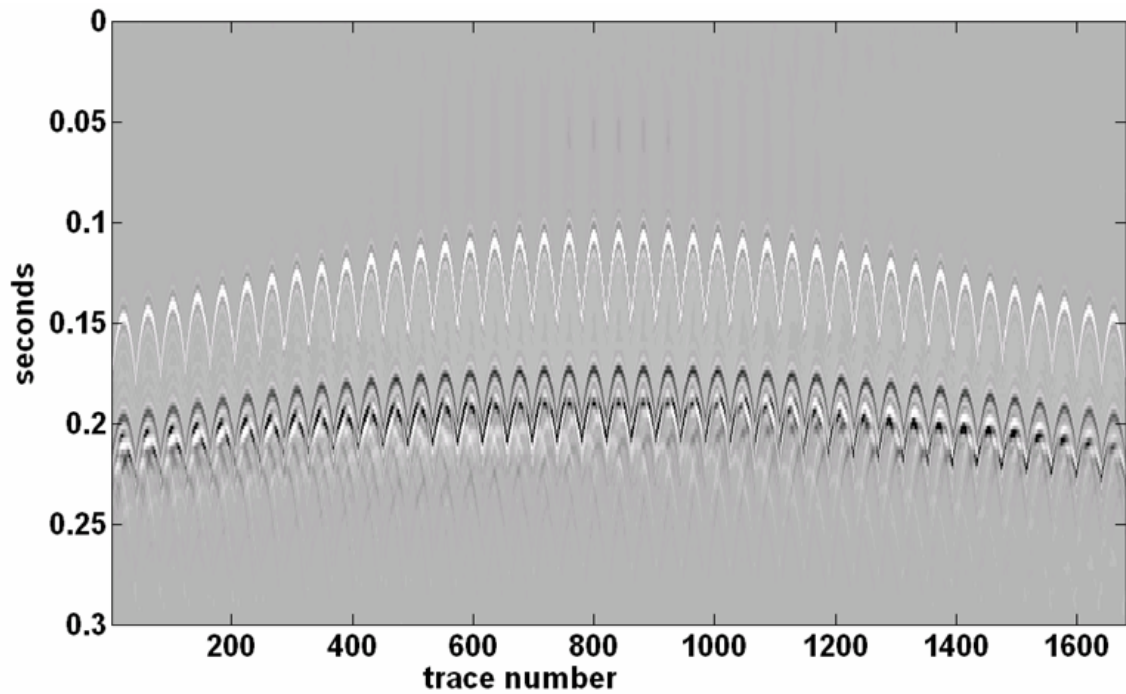
FIG. 8. An entire 3D shot record for a source location at the center of Figure 6. Each small hyperbolic event is a reflection as recorded on a line *y* =constant. The more complicated nature of the third reflector, compared to the first two, is readily apparent.
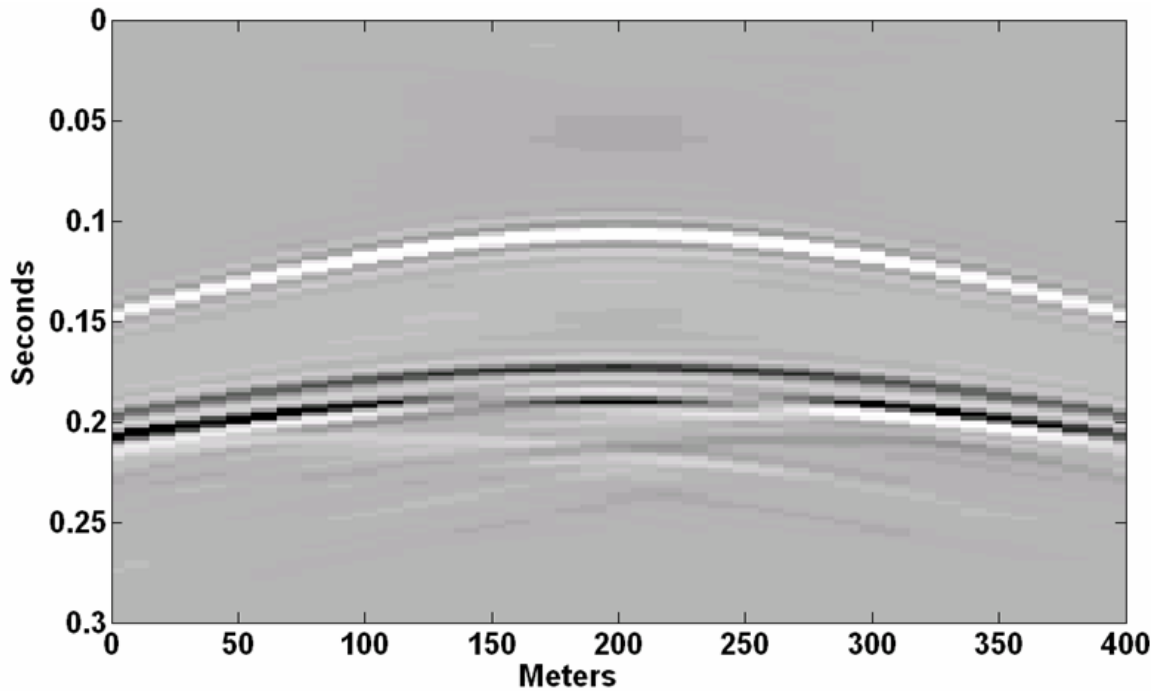
FIG. 9. The 3D response of Figure 8 is shown isolated along a single 2D receiver line at x=200.
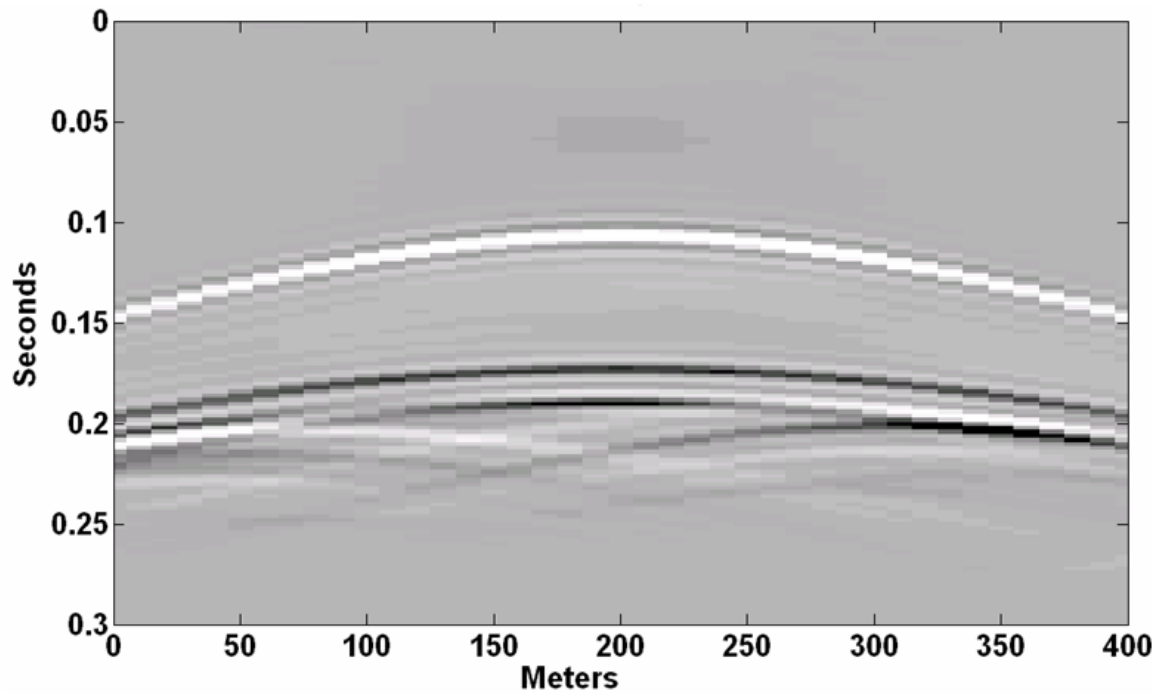
FIG. 10. The 3D response of Figure 8 is shown isolated along a single 2D line at y=200.
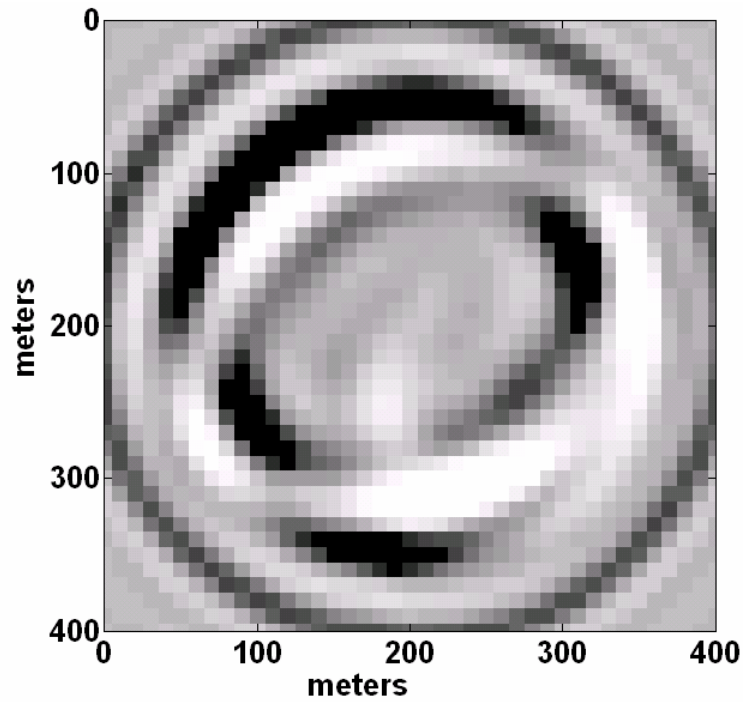
FIG. 11. A time slice at t=0.2 seconds through the 3D source record of Figure 8.
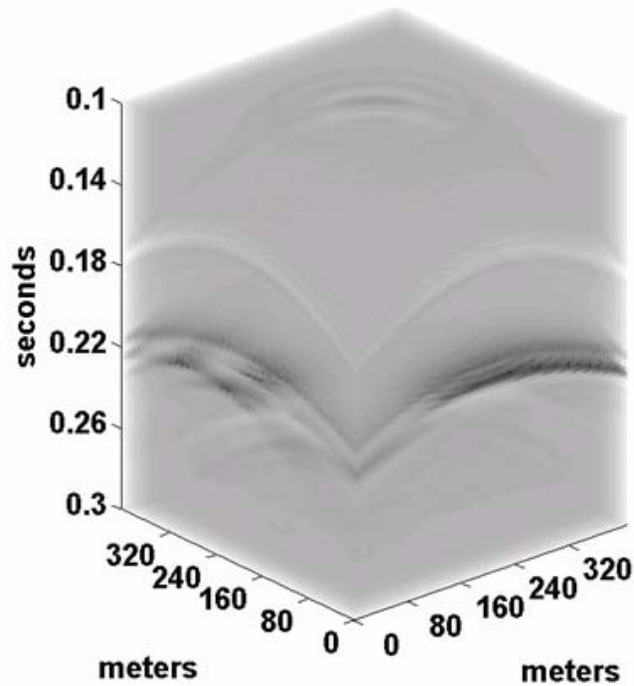
FIG. 12. The 3D source record of Figure 8 is shown in a true 3D perspective.

The 3D source records were migrated with a 3D Kirchhoff algorithm, as described in Cooper and Margrave (2007). Figures 13, 14, and 15 show depth slices corresponding to each of the three reflectors from the 3D migration of the source record of Figure 8. While the source record was sampled at 10m, these migrations are sampled at 5m. As mentioned previously, the modelling was actually done on a 5m grid and then downsampled, without antialias filtering, to the 10m receiver grid. Thus there is every reason to expect to see 5m detail in these migrated images. The 100 m reflector has produced an appropriately featureless image whose significant values are largely confined to the areal extent of the CMP coverage. The 180 m reflector, although it is featureless, has imaged with a very significant imprint from the nearby 200m reflector (Figure 14). As seen in Figure 15, the 200m reflector has produced a very good channel image, showing significant channel detail well outside the CMP coverage box.
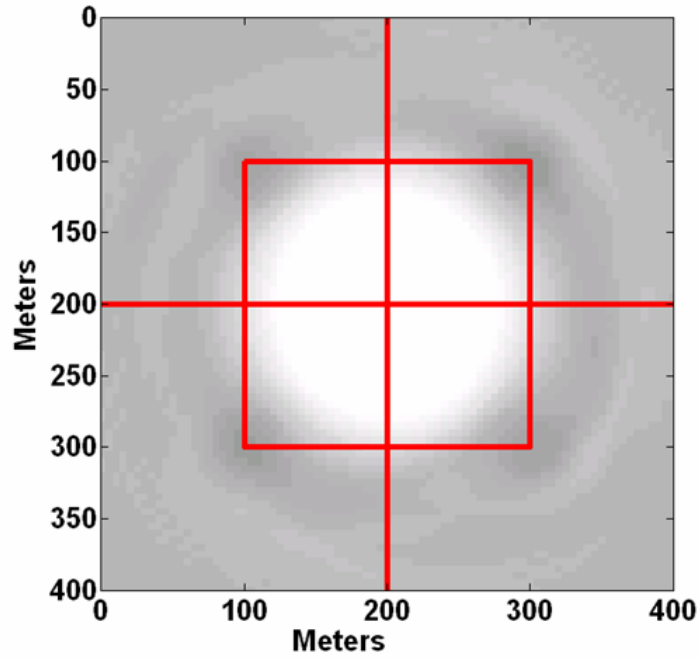
FIG. 13. A single depth slice at 100 m from a 3D migration of the data of Figure 8. The crossing red lines locate the source position and the red square denotes the boundary of the CMP's expected. This was modelled as a featureless reflector with a negative reflection coefficient.
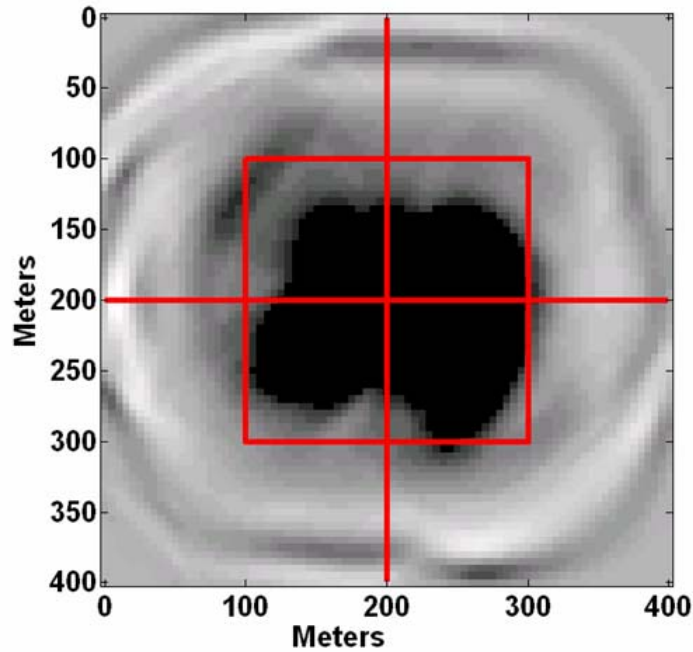
FIG. 14. Similar to Figure 13 except that the depth slice is at 180 m, where a featureless reflector with a positive reflection coefficient was modelled. The zero phase (non causal) wavelet has allowed the 200 m reflector (Figure 15) to influence this image.
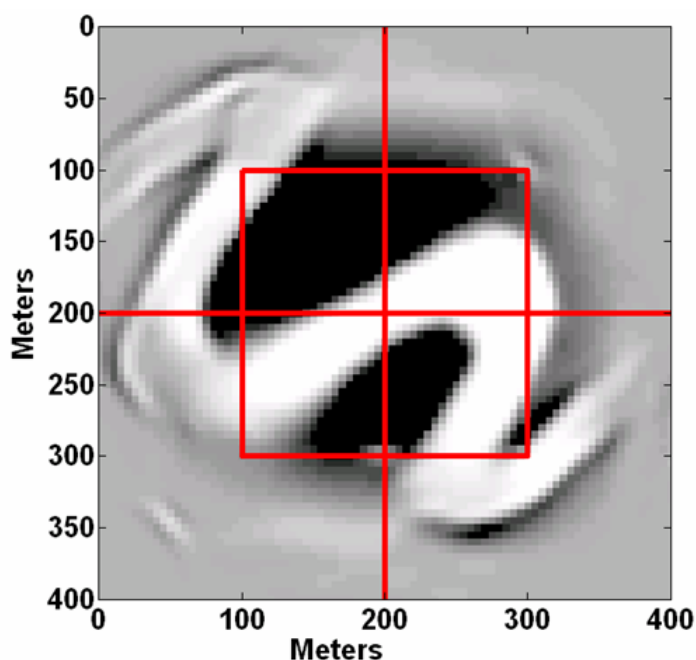
FIG. 15. Similar to Figures 13 and 14 except that the depth slice is at 200 m, where the reflector of Figure 6 was modelled.

Obviously space precludes showing even a tiny fraction of the 1681 source records in the exhaustive dataset, so we content ourselves to showing just one more. Figure 16 shows the 3D record for a source in the upper left-hand corner of the survey, that is at x = y = 0 in Figure 6. Compared to Figure 8, the significantly larger offsets and their one-sided nature are apparent. Figures 17 and 18 show 2D receiver lines sorted from the 3D gather and should be compared both to the channel reflector of Figure 6 and to the corresponding figures for the previous source record (Figures 9 and 10). Figure 19 is a time slice comparable to Figure 11. Finally, depth slices from the 3D migration are shown for each reflector in Figures 20, 21, and 22. Compared to Figure 13, the 100 m reflector has produced an image that has filled only about 50% of the CMP coverage box. The 180 m reflector (Figure 21) has also not filled the CMP box but there is a false channel image far outside the box. The 200m reflector has more fully filled the CMP box and has, in fact, imaged well beyond it.
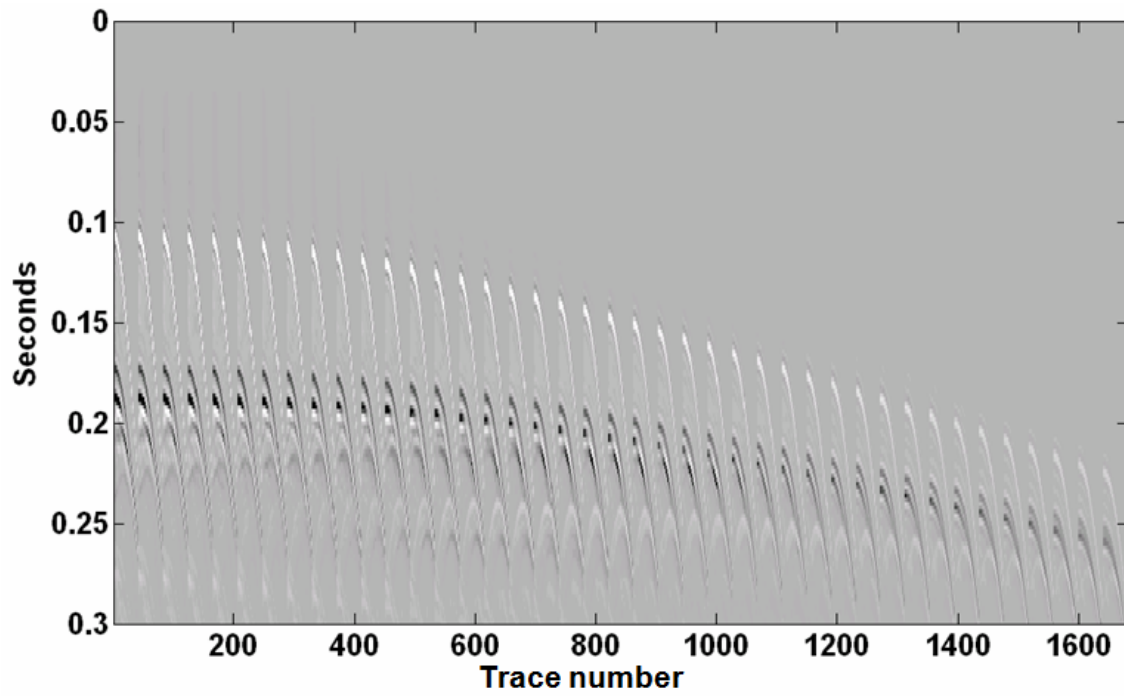
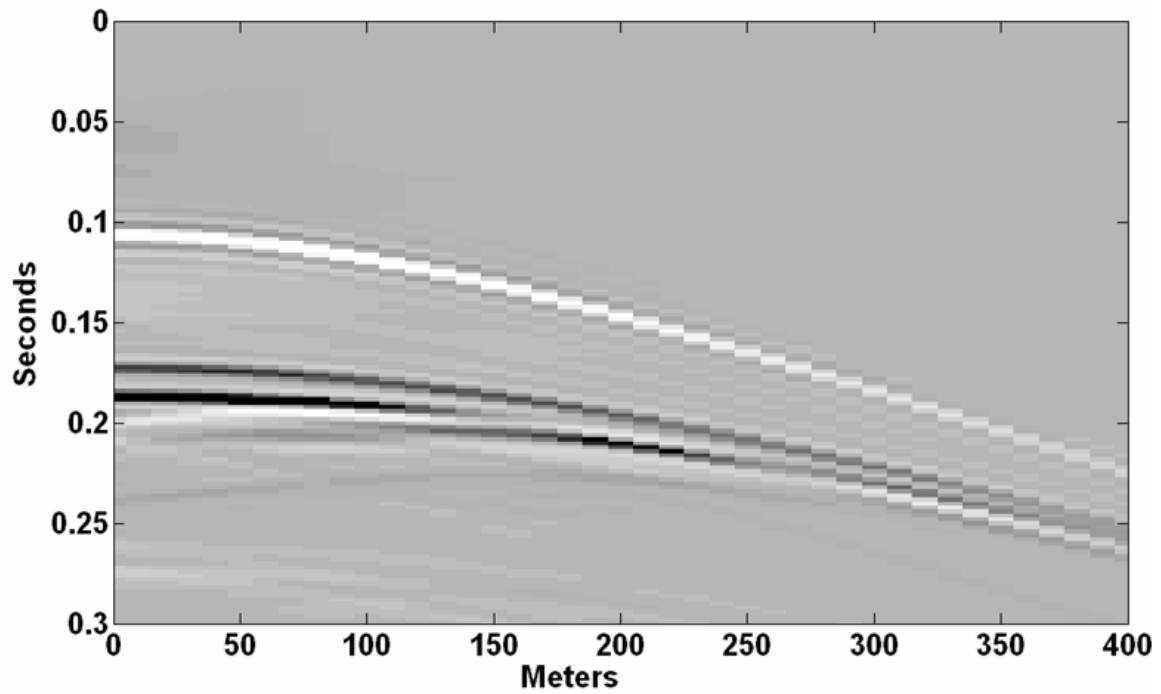FIG. 16. A 3D source record for a source located at x = y = 0 (Figure 6). Compare with Figure 8.

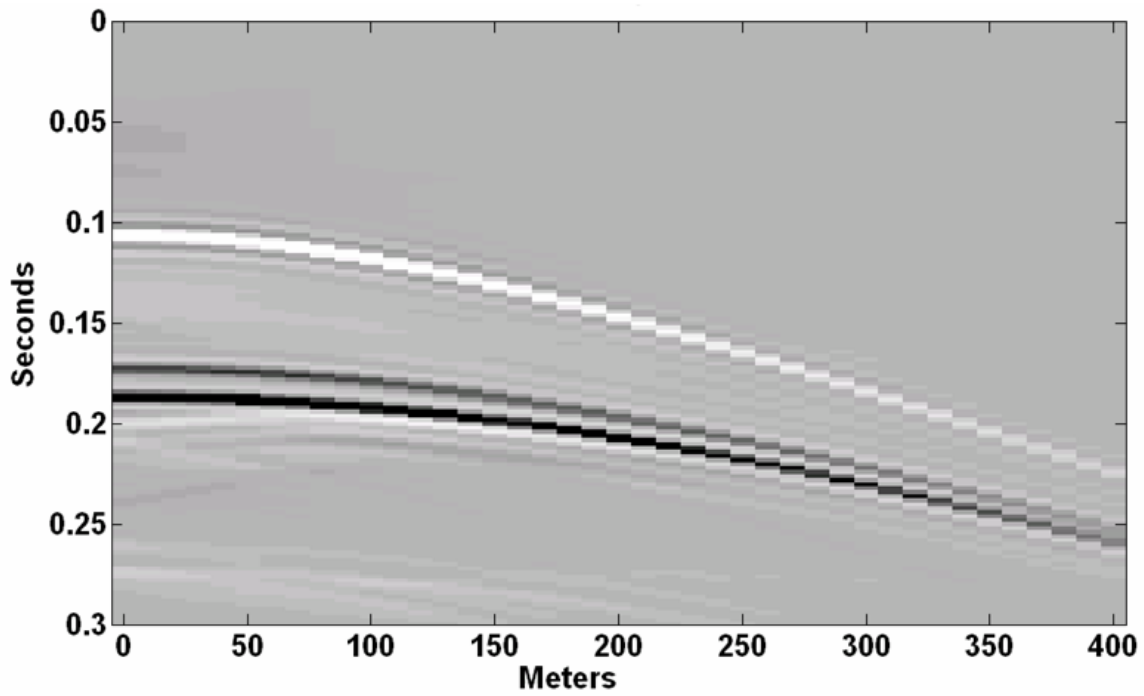FIG. 17. A 2D receiver line sorted from the data of Figure 16. The receivers were all at x=0.

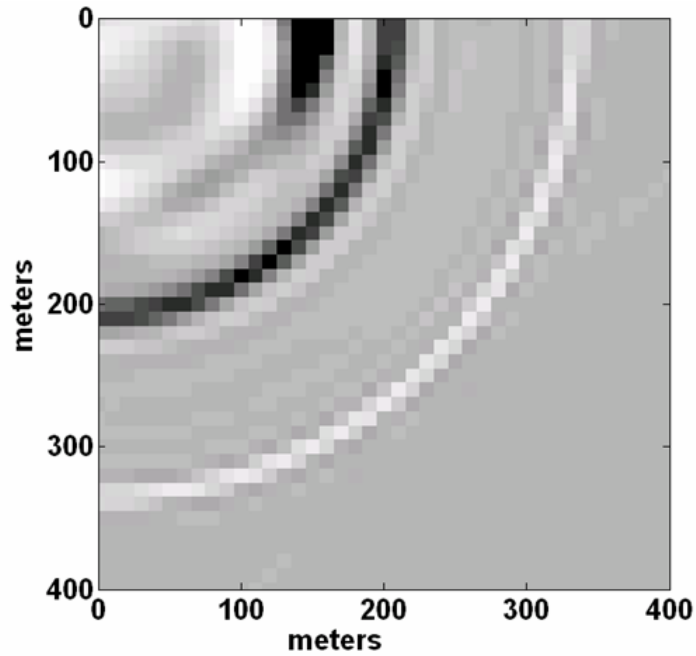FIG. 18. A 2D receiver line sorted from the data of Figure 16 for receivers at y=0.

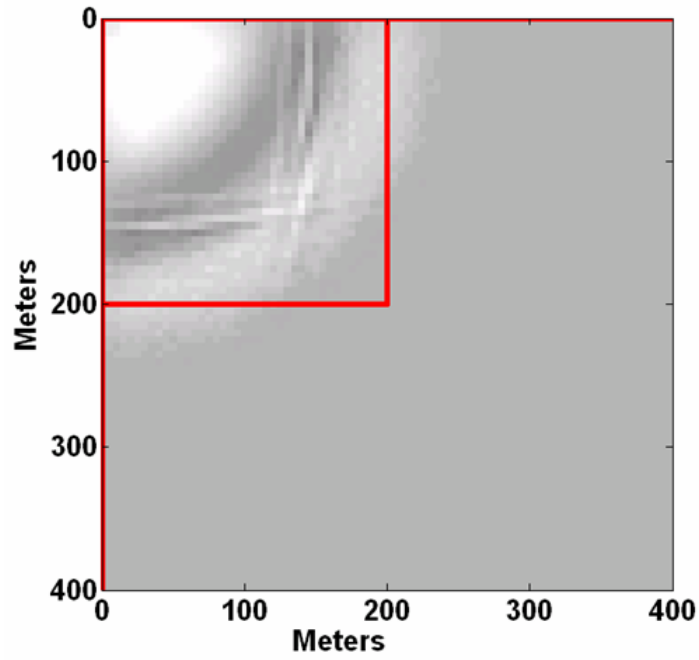FIG. 19. A time slice from the data of Figure 15, taken at t= 0.200 seconds.

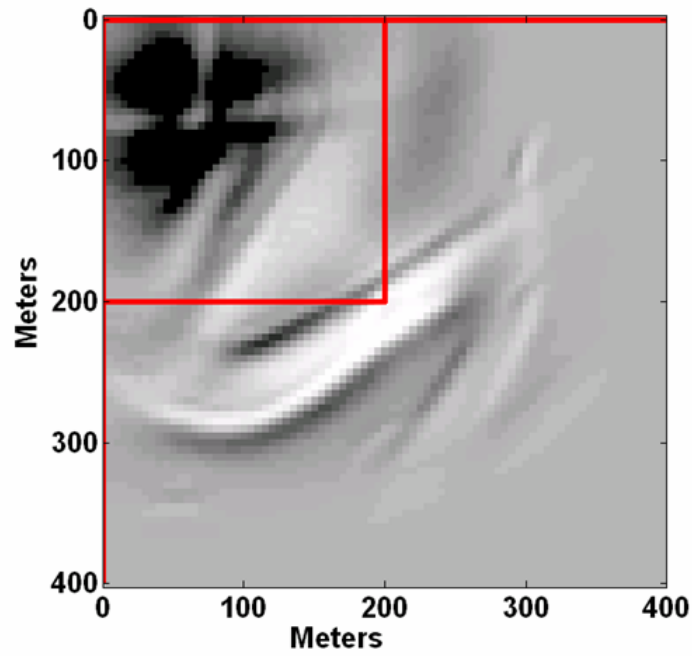FIG. 20. A depth slice at 100 m from the 3D migration of the data of Figure 16.

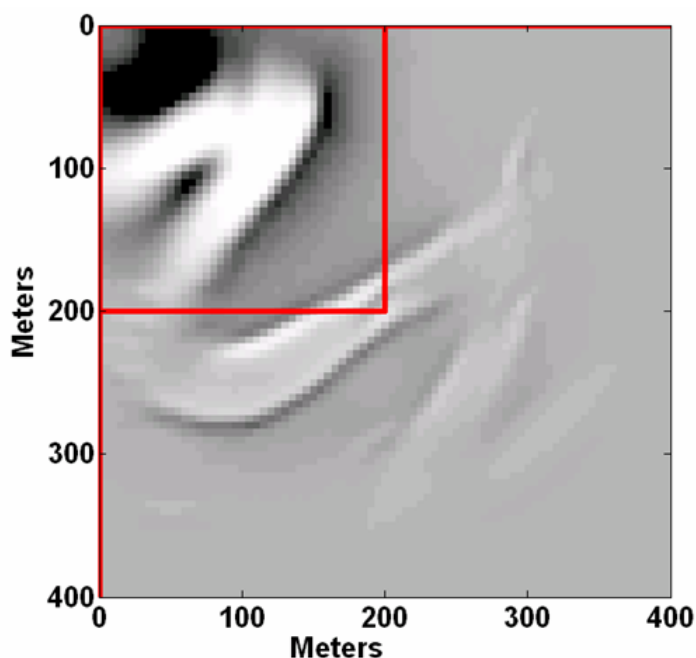FIG. 21. A depth slice at 180 m from the 3D migration of the data of Figure 16.

FIG. 22. A depth slice at 200m from the 3D migration of the data of Figure 16.

The entire 3D dataset was calculated in a single fast Linux workstation. One source record required about 150 seconds of CPU time and the entire calculation of all 1681 source records required 3 days. Kirchhoff migration of the exhaustive dataset, reported in Cooper and Margrave (2007), required 5 days with an algorithm that produced images only at three specific depth levels.

DISCUSSION AND CONCLUSIONS

Acoustic seismic modelling in 3D, using the Rayleigh-Sommerfeld theory of diffraction, has been described and demonstrated. The method was shown to be closely related to the more familiar Kirchhoff modelling and, when extended to a multi-reflector environment using the first-order Born approximation, is essentially phase-shift migration running in reverse. On theoretical principles, it is demonstrated that Kirchhoff modelling has a computational effort of $O\left(N^2\right)$ while Rayleigh-Sommerfeld is only $O\left(N\log N\right)$.

For each depth level from which a response is desired, a reflectivity map must be prepared that is specified on a grid that has half the spatial sample size of the desired receiver sampling. Then, for each reflective depth plane, the source wavefield is phase-shifted down to that depth, multiplied, point-by-point, by the reflectivity map, and then phase-shifted back to the surface. Although not specifically tested, it is anticipated that dipping reflectors can be modelled by simply transcribing their reflectivity signature onto a series of horizontal depth planes. The modelling theory was then applied to create an exhaustive 3D seismic dataset, which means that the dataset has no significant spatial aliasing in either source or receiver gathers. Careful examination of the resulting seismic response shows that the modelling technique produces very high-fidelity seismic models containing both reflection and diffraction events. Migration of the modelled data yielded very high resolution images of the reflective planes in the model. While the Rayleigh-

Sommerfeld technique as presented here does not model angle-dependent reflectivity, this would be possible with a modest extension by incorporating v(z) raytracing to build a table of incidence angle versus offset (from source to reflection point) for each reflector. It would also be possible to model lateral velocity variations using the same extensions that have been developed for phase-shift migration.

ACKNOWLEDGEMENTS

REFERENCES

Cooper, J. K., and Margrave, G. F., 2007, Simulations of 3D seismic acquisition footprint: CREWES Research Report, **19**.

Ersoy, O. K., 2007, Diffraction, Fourier optics, and imaging: Wiley-Interscience, ISBN-10: 0-471-23816-3, 413 pages.

Shearer, P. M., 1999, Introduction to Seismology: Cambridge University Press, ISBN 0-521-66953-7, 260 pages.